Hindawi
Mathematical Problems in Engineering
Volume 2019, Article ID 8678473, 14 pages
https://doi.org/10.1155/2019/8678473

*Research Article*

# Robust Adaptive Relative Position and Attitude Control for Noncooperative Spacecraft Hovering under Coupled Uncertain Dynamics

**Jianghui Liu**,[1] **Haiyang Li**,[1] **YaKun Zhang**,[2] **Jianyong Zhou**,[1] **Lin Lu**,[1] **and Fuqi Li**[3]

[1]*College of Aerospace Science and Engineering, National University of Defense Technology, Changsha, Hunan 410073, China*
[2]*Department of Electronic and Optical Engineering, Space Engineering University, Beijing 101416, China*
[3]*The PLA Unit 91395, Beijing 102401, China*

Correspondence should be addressed to Haiyang Li; lihaiyang@nudt.edu.cn

Received 22 April 2019; Revised 22 September 2019; Accepted 15 November 2019; Published 28 December 2019

Academic Editor: Xuping Zhang



The control of body-fixed hovering over noncooperative target, as one of the key problems of relative motion control between spacecrafts, is studied in the paper. The position of the chaser in the noncooperative target's body coordinate system is required to remain unchanged, and the attitude of the chaser and the target must be synchronized at the same time. Initially, a six-degrees-of-freedom-coupled dynamic model of a chaser relative to a target is established, and relative attitude dynamics is described through using modified Rodrigues parameters (MRP). Considering the model uncertainty and external disturbances of the noncooperative target system, an adaptive nonsingular terminal sliding mode (NTSM) controller is designed. Adaptive tuning method is used to overcome the effects of the model uncertainty and external disturbances. The upper bounds of the model uncertainty and external disturbances are not required to be known in advance. The actual control law is continuous and chatter-free, which is obtained by integrating the discontinuous derivative control signal. Finally, these theoretical results are verified by numerical simulation.

## 1. Introduction

On-orbit spacecraft is of great value. When breaking down in space, on-orbit repair, component replacement, and refueling can significantly prevent further cost of replacing a new one [1–6]. Therefore, it has drawn much attention from researchers. Relative hovering usually indicates that a spacecraft stays fixed in its position and attitude in the body coordinate system of another spacecraft. The state of relative hovering greatly facilitates space surveillance and inspections.

Historically, related research studies have mainly focused on the hovering over asteroids. Scheeres first proposed the concept of hovering orbit of the spacecraft relative to asteroids in 1999 [7]. In general, hovering over an asteroid mainly includes inertial hovering and body-fixed hovering [8, 9]. Broschart simulated the hovering control of an asteroid under slight gravity and determined the stable region of inertial hovering [8]. In the control of hovering over asteroids, the spacecraft needs to continuously apply the control thrust to counteract the gravity and rotational acceleration to maintain the desired position [9, 10]. This method is feasible on asteroids due to low nominal acceleration of the spacecraft [7, 8, 11]. Zeng proposed the solar sail spacecraft's hover over an asteroid, which greatly extended the hover time and hover range without fuel consumption [12]. It should be pointed out that the research on spacecraft hovering over an asteroid in the early stage mainly concentrated on the relative position control of the spacecraft and asteroid irrespective of the relative attitude control [7–9, 11, 13–15]. Lee et al. put forward passive tracking control of the relative position and relative attitude of hovering over an asteroid in the framework of geometric mechanics [16]. Aiming at the orbit and attitude control of

hovering over a rotating asteroid at a low speed, Lee et al. designed a continuous finite-time convergence control scheme [17, 18].

Strictly speaking, the situation of a spacecraft hovering over an asteroid is different from that of hovering over the target spacecraft. This is because the former is influenced by the gravity from both the asteroid and the sun, while the latter is only influenced by Earth's gravity. Therefore, the dynamic equations in the two cases are also different.

In this paper, we mainly study the hovering control of one spacecraft relative to another spacecraft. Recently, some researchers have also published many findings concerning hovering control between two spacecrafts. Tan analyzed and solved the relative motions of the two spacecrafts in the near circle and elliptical orbits, respectively. The controller was designed using generalized inverse matrix transformation, and the guidance deviation was obtained by model prediction [19, 20]. Xue has established a hybrid system model for relative hovering between the two spacecrafts [21]. Based on the description of the state transfer matrix between the two spacecrafts, Cheng used a multipulse control method to study the relative hovering motion [22]. To solve the problem of hovering between the two spacecrafts at superclose distance, Xu proposed the control method of line of sight pointing tracking on the basis of relative orbit control and realized the joint control of the relative orbit and attitude [23]. Song studied the hovering closed-loop control method based on Hill equation [24]. Dang established a precise analytical solution for hovering between the two spacecrafts and deduced the minimum force and minimum fuel positions during the orbital period [25]. Huang studied the problem of finite-time hovering control in the absence of the radial or in-track thrust [26].

However, previous research studies on hovering control mainly focused on the control of the relative position between the two spacecrafts. There are few research studies on relative attitude control, and hovering control is mostly in the form of open-loop control. Even if the relative attitude control problem is considered, it is restricted to the condition of the stable attitude or slow attitude change of the target, and the relative position and relative attitude are also controlled separately, ignoring their coupling. Further complicating things, the model parameters of the spacecraft are not likely to be precisely known during hovering operations, and the spacecraft is always subject to external environment disturbances [27–29]. Sun investigates relative position and attitude control for spacecraft rendezvous and proximity operations subject to input saturation, kinematic couplings, parametric uncertainties, and unknown external disturbances. State feedback control method [30], disturbance-observer-based robust nonlinear control scheme [31], a six-degrees-of-freedom integrated adaptive fuzzy nonlinear control method [32], and robust adaptive control approach [33] are proposed. The terminal sliding mode control (TSMC) method based on the conventional sliding mode control (SMC) method has the advantage of finite-time convergence [34]. Its sliding mode is independent of the model parameters and external disturbances, and thus has been widely used in nonlinear control [35, 36]. However, the disadvantage is that the nonlinear term used in the TSMC may cause a singularity problem leading to a control magnitude to become unbounded. In order to solve this problem, Feng proposed the nonsingular terminal sliding mode control (NTSMC) method [37, 38]. Nonsingular terminal sliding mode controllers are now widely used in a variety of application areas like robotics [39–41], aerospace, and process control [42, 43].

Considering the limitations of previous studies, it is necessary to further study hovering control between the two spacecrafts. In this paper, control problem of the chaser hovering over the target with relatively rapid attitude change in space is studied. A nonlinear six-degrees-of-freedom-coupled dynamic model is established in the chaser's body coordinate system. A chattering-free adaptive nonsingular terminal sliding mode (NTSM) controller is designed. Firstly, the conventional sliding surface is established, and then the nonsingular terminal sliding surface is constructed on this basis. The adaptive tuning method is used to deal with the model uncertainty and external disturbances. The upper bounds of the model uncertainty and external disturbances are not required to be known in advance [44–46]. The actual control law is continuous and chatter-free, which is obtained by integrating the discontinuous derivative control signal.

The rest of the sections are as follows. Section 2 introduces dynamics for the chaser and the target. Section 3 presents the designs of the adaptive nonsingular terminal sliding mode (NTSM) controller and demonstrates the stability of the closed-loop system. Simulation studies performed on the relative position and attitude control of the hovering example are presented in Section 4. Section 5 draws conclusions.

## 2. Dynamics for the Chaser and the Target

In this paper, the skew-symmetric matrix $S(\boldsymbol{\zeta}) \in \mathbb{R}^{3\times3}$ derived from a vector $\boldsymbol{\zeta} = [\,\zeta_1 \;\; \zeta_2 \;\; \zeta_3\,]^{\mathrm{T}} \in \mathbb{R}^3$ is defined as

$$S(\boldsymbol{\zeta}) = \begin{bmatrix} 0 & -\zeta_3 & \zeta_2 \\ \zeta_3 & 0 & -\zeta_1 \\ -\zeta_2 & \zeta_1 & 0 \end{bmatrix}, \tag{1}$$

and it satisfies $\boldsymbol{\zeta}^{\mathrm{T}} S(\boldsymbol{\zeta}) = 0$, $S(\boldsymbol{\zeta})\boldsymbol{\xi} = -S(\boldsymbol{\xi})\boldsymbol{\zeta}$, $\boldsymbol{\xi}^{\mathrm{T}} S(\boldsymbol{\zeta})\boldsymbol{\xi} = 0$ for any $\boldsymbol{\xi} = [\,\xi_1 \;\; \xi_2 \;\; \xi_3\,]^{\mathrm{T}} \in \mathbb{R}^3$.

$\mathrm{sgn}(\mathbf{s}) = [\mathrm{sgn}(s_1), \cdots, \mathrm{sgn}(s_n)]^{\mathrm{T}}$ for any $\mathbf{s} = [s_1, \cdots, s_n]^{\mathrm{T}} \in \mathbb{R}^n$, where

$$\mathrm{sgn}(s_i) = \begin{cases} -1, & s_i < 0, \\ 0, & s_i = 0, \\ 1, & s_i > 0. \end{cases} \tag{2}$$

*2.1. Dynamics for Relative Orbit.* The relative motion scenario between the chaser and the target is shown in Figure 1. $F_E = \{O_E X_E Y_E Z_E\}$ is the Earth-centered inertial frame, with its coordinate origin at the Earth center and nonrotating with respect to the stars. The $O_E X_E$ axis points in the

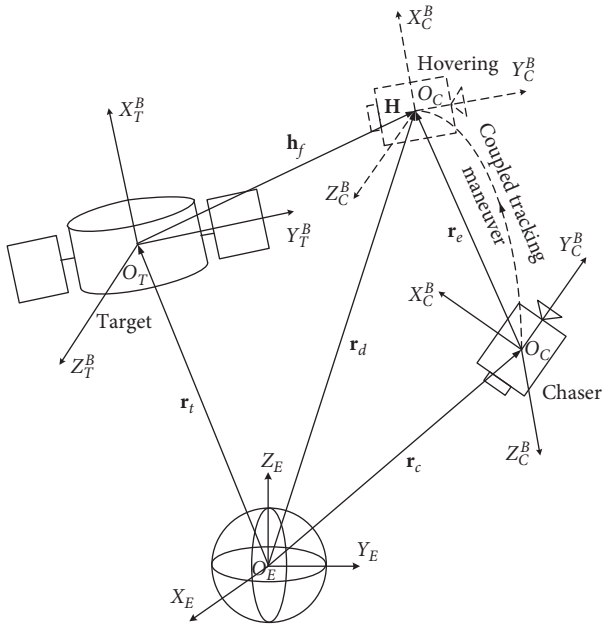


Figure 1: Relative position and attitude motion coordinate system.

direction of the Earth's vernal equinox. The $O_E Z_E$ axis points to the direction of North Pole. The direction of $O_E Y_E$ axis is determined by the right-hand rule. $F_T = \{O_T X_T^B Y_T^B Z_T^B\}$ and $F_C = \{O_C X_C^B Y_C^B Z_C^B\}$ are the body frames of the target and the chaser, respectively. The body frame is fixed onto the spacecraft body and rotates with it. $\{\mathbf{r}_c, \mathbf{r}_e\}$ is the position vectors in the frame $F_C$, and $\{\mathbf{r}_t, \mathbf{r}_d, \mathbf{h}_f\}$ is the position vectors in the frame $F_T$.

The position and attitude dynamic model of the chaser relative to the frame $F_E$ is [47]

$$\begin{cases} \dot{r}_c = \mathbf{v}_c - S(\boldsymbol{\omega}_c)\mathbf{r}_c, \\ \dot{\sigma}_c = \dfrac{1}{4}\left[\left(1 - \boldsymbol{\sigma}_c^{\mathrm{T}}\boldsymbol{\sigma}_c\right)\mathbf{I}_3 + 2\boldsymbol{\sigma}_c\boldsymbol{\sigma}_c^{\mathrm{T}} + 2S(\boldsymbol{\sigma}_c)\right]\boldsymbol{\omega}_c, \\ m_c\dot{v}_c + m_c S(\boldsymbol{\omega}_c)\mathbf{v}_c = \mathbf{F}_c + \mathbf{F}_d, \\ \mathbf{J}_c\dot{\omega}_c + S(\boldsymbol{\omega}_c)\mathbf{J}_c\boldsymbol{\omega}_c = \boldsymbol{\tau}_c + \boldsymbol{\tau}_d, \end{cases} \tag{3}$$

where $\mathbf{v}_c \in \mathbb{R}^3$ and $\boldsymbol{\omega}_c \in \mathbb{R}^3$ are the chaser's velocity and angular velocity, respectively. $\mathbf{r}_c \in \mathbb{R}^3$ is the chaser's position, and $\boldsymbol{\sigma}_c \in \mathbb{R}^3$ is the modified Rodrigues parameter (MRP) vector to describe the attitude of frame $F_C$ with respect to frame $F_E$. $\mathbf{J}_c \in \mathbb{R}^{3\times3}$ and $m_c \in \mathbb{R}$ are the chaser's inertial matrix and mass, respectively. $\mathbf{F}_c \in \mathbb{R}^3$ and $\boldsymbol{\tau}_c \in \mathbb{R}^3$ are the chaser's control force and control torque, respectively. $\mathbf{F}_d \in \mathbb{R}^3$ and $\boldsymbol{\tau}_d \in \mathbb{R}^3$ are unknown bounded disturbance force and unknown bounded disturbance torque of the chaser, respectively. They are all expressed in the frame $F_C$.

Ignoring the external forces and torques, the position and attitude dynamic model of the noncooperative target relative to the frame $F_E$ is [31]

$$\begin{cases} \dot{r}_t = \mathbf{v}_t - S(\boldsymbol{\omega}_t)\mathbf{r}_t, \\ \dot{\sigma}_t = \dfrac{1}{4}\left[\left(1 - \boldsymbol{\sigma}_t^{\mathrm{T}}\boldsymbol{\sigma}_t\right)\mathbf{I}_3 + 2\boldsymbol{\sigma}_t\boldsymbol{\sigma}_t^{\mathrm{T}} + 2S(\boldsymbol{\sigma}_t)\right]\boldsymbol{\omega}_t, \\ \dot{v}_t + S(\boldsymbol{\omega}_t)\mathbf{v}_t = \mathbf{0}, \\ \mathbf{J}_t\dot{\omega}_t + S(\boldsymbol{\omega}_t)\mathbf{J}_t\boldsymbol{\omega}_t = \mathbf{0}, \end{cases} \tag{4}$$

where $\mathbf{v}_t \in \mathbb{R}^3$ and $\boldsymbol{\omega}_t \in \mathbb{R}^3$ are the target's velocity and angular velocity, respectively. $\mathbf{r}_t \in \mathbb{R}^3$ is the target's position, and $\boldsymbol{\sigma}_t \in \mathbb{R}^3$ is the attitude of frame $F_T$ with respect to frame $F_E$. $\mathbf{J}_t \in \mathbb{R}^{3\times3}$ and $m_t \in \mathbb{R}$ are the target's inertial matrix and mass, respectively. They are all expressed in the frame $F_T$.

*2.2. Relative Dynamic Model.* The relative attitude $\boldsymbol{\sigma}_e \in \mathbb{R}^3$ of frame $F_C$ with respect to frame $F_T$ described by MRP is [48]

$$\boldsymbol{\sigma}_e = \frac{\boldsymbol{\sigma}_c\left(1 - \boldsymbol{\sigma}_t^{\mathrm{T}}\boldsymbol{\sigma}_t\right) + \boldsymbol{\sigma}_t\left(\boldsymbol{\sigma}_c^{\mathrm{T}}\boldsymbol{\sigma}_c - 1\right) - 2S(\boldsymbol{\sigma}_t)\boldsymbol{\sigma}_c}{1 + 2\boldsymbol{\sigma}_t^{\mathrm{T}}\boldsymbol{\sigma}_c + \boldsymbol{\sigma}_t^{\mathrm{T}}\boldsymbol{\sigma}_t\boldsymbol{\sigma}_c^{\mathrm{T}}\boldsymbol{\sigma}_c}. \tag{5}$$

The corresponding attitude transfer matrix $\mathbf{M}_e \in \mathbb{R}^{3\times3}$ is

$$\mathbf{M}_e = \mathbf{I}_3 + \frac{8S(\boldsymbol{\sigma}_e)S(\boldsymbol{\sigma}_e) - 4\left(1 - \boldsymbol{\sigma}_e^{\mathrm{T}}\boldsymbol{\sigma}_e\right)S(\boldsymbol{\sigma}_e)}{\left(1 + \boldsymbol{\sigma}_e^{\mathrm{T}}\boldsymbol{\sigma}_e\right)^2}, \tag{6}$$

where $\mathbf{I}_3 \in \mathbb{R}^{3\times3}$ is a unit matrix. It can be seen from Figure 1 that the position and velocity of the hovering point $\mathbf{H}$ described in the frame $F_T$ are

$$\mathbf{r}_d = \mathbf{r}_t + \mathbf{h}_f, \tag{7}$$

$$\mathbf{v}_d = \mathbf{v}_t + S(\boldsymbol{\omega}_t)\mathbf{h}_f. \tag{8}$$

The relative angular velocity, relative position, and relative velocity of the two spacecrafts described in the frame $F_C$ are

$$\boldsymbol{\omega}_e = \boldsymbol{\omega}_c - \mathbf{M}_e\boldsymbol{\omega}_t, \tag{9}$$

$$\mathbf{r}_e = \mathbf{r}_c - \mathbf{M}_e\mathbf{r}_t, \tag{10}$$

$$\mathbf{v}_e = \mathbf{v}_c - \mathbf{M}_e\mathbf{v}_t. \tag{11}$$

Substituting equations (9)~(11) into equation (3) and using the equations $\dot{\mathbf{M}}_e = -S(\boldsymbol{\omega}_e)\mathbf{M}_e$, $\dot{r}_d = \mathbf{v}_d - S(\boldsymbol{\omega}_t)\mathbf{r}_d$ and $\mathbf{M}_e^{-1} = \mathbf{M}_e^{\mathrm{T}}$, the relative motion equations described in the frame $F_C$ can be derived:

$$\begin{cases} \dot{\mathbf{r}}_e = \mathbf{v}_e - S(\boldsymbol{\omega}_c)\mathbf{r}_e, \\ \dot{\boldsymbol{\sigma}}_e = G(\boldsymbol{\sigma}_e)\boldsymbol{\omega}_e, \\ m_c\dot{v}_e = -m_c\left[S(\boldsymbol{\omega}_c)\mathbf{v}_c + \mathbf{M}_e\dot{v}_d - S(\boldsymbol{\omega}_e)\left(\mathbf{v}_c - \mathbf{v}_e\right)\right] + \mathbf{F}_c + \mathbf{F}_d, \\ \mathbf{J}_c\dot{\omega}_e = -S(\boldsymbol{\omega}_c)\mathbf{J}_c\boldsymbol{\omega}_c - \mathbf{J}_c\left[\mathbf{M}_e\dot{\omega}_t + S(\boldsymbol{\omega}_c)\boldsymbol{\omega}_e\right] + \boldsymbol{\tau}_c + \boldsymbol{\tau}_d, \end{cases} \tag{12}$$

where $G(\boldsymbol{\sigma}_e) = [(1 - \boldsymbol{\sigma}_e^{\mathrm{T}}\boldsymbol{\sigma}_e)\mathbf{I}_3 + 2\boldsymbol{\sigma}_e\boldsymbol{\sigma}_e^{\mathrm{T}} + 2S(\boldsymbol{\sigma}_e)]/4$ is a nonsingular matrix. From equations (4) and (8)–(11) and $\mathbf{M}_e S(\boldsymbol{\zeta}) = -S(\mathbf{M}_e\boldsymbol{\zeta})\mathbf{M}_e$, $\mathbf{M}_e\dot{v}_d$ can be derived as

$$\begin{aligned}\mathbf{M}_e\dot{\upsilon}_d &= \mathbf{M}_e\left[\dot{\upsilon}_t + S(\dot{\omega}_t)\mathbf{h}_f\right]\\ &= -\mathbf{M}_e S(\boldsymbol{\omega}_t)\boldsymbol{\upsilon}_t - \mathbf{M}_e S\left(\mathbf{h}_f\right)\dot{\omega}_t\\ &= -S(\mathbf{M}_e\boldsymbol{\omega}_t)\left[\mathbf{M}_e\boldsymbol{\upsilon}_d - \mathbf{M}_e S(\boldsymbol{\omega}_t)\mathbf{h}_f\right] - \mathbf{M}_e S\left(\mathbf{h}_f\right)\dot{\omega}_t\\ &= -S(\boldsymbol{\omega}_c - \boldsymbol{\omega}_e)\left[\boldsymbol{\upsilon}_c - \boldsymbol{\upsilon}_e - S(\boldsymbol{\omega}_c - \boldsymbol{\omega}_e)\mathbf{M}_e\mathbf{h}_f\right]\\ &\quad - \mathbf{M}_e S\left(\mathbf{h}_f\right)\dot{\omega}_t.\end{aligned} \tag{13}$$

Also, $\dot{\boldsymbol{\omega}}_t$ in equation (13) can be calculated by equations (4) and (9):

$$\begin{aligned}\dot{\boldsymbol{\omega}}_t &= -\mathbf{J}_t^{-1}S(\boldsymbol{\omega}_t)\mathbf{J}_t\boldsymbol{\omega}_t\\ &= -\mathbf{J}_t^{-1}S\left(\mathbf{M}_e^{\mathrm{T}}(\boldsymbol{\omega}_c - \boldsymbol{\omega}_e)\right)\mathbf{J}_t\mathbf{M}_e^{\mathrm{T}}(\boldsymbol{\omega}_c - \boldsymbol{\omega}_e).\end{aligned} \tag{14}$$

Therefore, equation (12) can be rewritten as

$$\begin{cases}\dot{\mathbf{r}}_e = \boldsymbol{\upsilon}_e - S(\boldsymbol{\omega}_c)\mathbf{r},\\ \dot{\boldsymbol{\sigma}}_e = G(\boldsymbol{\sigma}_e)\boldsymbol{\omega}_e,\\ m_c\dot{\boldsymbol{\upsilon}}_e = -m_c\mathbf{P}_1 - \mathbf{P}_2 + \mathbf{F}_c + \mathbf{F}_d,\\ \mathbf{J}_c\dot{\boldsymbol{\omega}}_e = -S(\boldsymbol{\omega}_c)\mathbf{J}_c\boldsymbol{\omega}_c - \mathbf{J}_c S(\boldsymbol{\omega}_c)\boldsymbol{\omega}_e + \mathbf{P}_3 + \boldsymbol{\tau}_c + \boldsymbol{\tau}_d,\end{cases} \tag{15}$$

where

$$\begin{aligned}\mathbf{P}_1 &= S(\boldsymbol{\omega}_c)\boldsymbol{\upsilon}_e + S^2(\boldsymbol{\omega}_c - \boldsymbol{\omega}_e)\mathbf{M}_e\mathbf{h}_f,\\ \mathbf{P}_2 &= m_c\mathbf{M}_e S\left(\mathbf{h}_f\right)\mathbf{J}_t^{-1}S\left(\mathbf{M}_e^{\mathrm{T}}(\boldsymbol{\omega}_c - \boldsymbol{\omega}_e)\right)\mathbf{J}_t\mathbf{M}_e^{\mathrm{T}}(\boldsymbol{\omega}_c - \boldsymbol{\omega}_e),\\ \mathbf{P}_3 &= \mathbf{J}_c\mathbf{M}_e\mathbf{J}_t^{-1}S\left(\mathbf{M}_e^{\mathrm{T}}(\boldsymbol{\omega}_c - \boldsymbol{\omega}_e)\right)\mathbf{J}_t\mathbf{M}_e^{\mathrm{T}}(\boldsymbol{\omega}_c - \boldsymbol{\omega}_e).\end{aligned} \tag{16}$$

*2.3. Integrated Dynamic Model.* Defining state variables $\mathbf{e}_1 = [\mathbf{r}_e^{\mathrm{T}}, \boldsymbol{\sigma}_e^{\mathrm{T}}]^{\mathrm{T}}$ and $\mathbf{e}_2 = [\boldsymbol{\upsilon}_e^{\mathrm{T}}, \boldsymbol{\omega}_e^{\mathrm{T}}]^{\mathrm{T}}$ from equation (15) yields

$$\dot{\mathbf{e}}_1 = \mathbf{A}_1\mathbf{e}_1 + \mathbf{A}_2\mathbf{e}_2, \tag{17}$$

$$\mathbf{M}\dot{\mathbf{e}}_2 = \mathbf{B}_1 + \mathbf{B}_2 + \mathbf{u} + \mathbf{d}, \tag{18}$$

$$\begin{aligned}\mathbf{A}_1 &= \begin{bmatrix}-S(\boldsymbol{\omega}_c) & \mathbf{0}_3\\ \mathbf{0}_3 & \mathbf{0}_3\end{bmatrix},\\ \mathbf{A}_2 &= \begin{bmatrix}\mathbf{I}_3 & \mathbf{0}_3\\ \mathbf{0}_3 & G(\boldsymbol{\sigma}_e)\end{bmatrix},\\ \mathbf{M} &= \begin{bmatrix}m_c\mathbf{I}_3 & \mathbf{0}_3\\ \mathbf{0}_3 & J_c\end{bmatrix},\\ \mathbf{B}_1 &= \begin{bmatrix}-m_c\mathbf{P}_1\\ -S(\boldsymbol{\omega}_c)J_c\boldsymbol{\omega}_c - J_c S(\boldsymbol{\omega}_c)\boldsymbol{\omega}_e\end{bmatrix},\\ \mathbf{B}_2 &= \begin{bmatrix}\mathbf{P}_2\\ \mathbf{P}_3\end{bmatrix},\\ \mathbf{u} &= \begin{bmatrix}\mathbf{F}_c\\ \boldsymbol{\tau}_c\end{bmatrix},\\ \mathbf{d} &= \begin{bmatrix}\mathbf{F}_d\\ \boldsymbol{\tau}_d\end{bmatrix}.\end{aligned} \tag{19}$$

*Remark 1.* $\mathbf{A}_1$ in model (17) and $\mathbf{B}_1$ in model (18) reflect that the relative position motion between the two spacecrafts is affected by the relative attitude motion, which indicates that there is a strong coupling effect between relative attitude and relative position.

This paper aims to design a controller so that the chaser reaches a predetermined hovering point $\mathbf{H}$, and the relative attitude between the two spacecrafts is $\boldsymbol{\sigma}_e = \boldsymbol{\sigma}_{e0}$, $\boldsymbol{\sigma}_{e0}$ is a constant. In order to facilitate the analysis, the relative attitude is $\boldsymbol{\sigma}_{e0} = \mathbf{0}_{3\times1}$, that is, the attitude between the two spacecrafts is synchronized. From equations (5), (9)–(11), (17), and (18), we can see that the control goal is equivalent to designing the control input $\mathbf{u}$ to satisfy $\lim_{t\longrightarrow\infty}\|\mathbf{e}_1(t)\| \le \phi_1$ and $\lim_{t\longrightarrow\infty}\|\mathbf{e}_2(t)\| \le \phi_2$, where $\phi_1$ and $\phi_2$ are any small positive numbers.

## 3. Controller Design and Stability Analysis

Considering the model uncertainty of the system, from equation (18) yields

$$(\mathbf{M}_d + \Delta\mathbf{M})\dot{e}_2 = \mathbf{B}_{d1} + \Delta\mathbf{B}_1 + \mathbf{B}_{d2} + \Delta\mathbf{B}_2 + \mathbf{u} + \mathbf{d}, \tag{20}$$

where $\mathbf{M}_d \in \mathbb{R}^{6\times6}$, $\mathbf{B}_{d1} \in \mathbb{R}^6$, and $\mathbf{B}_{d2} \in \mathbb{R}^6$ are the nominal model of the system. $\Delta\mathbf{M} \in \mathbb{R}^{6\times6}$, $\Delta\mathbf{B}_1 \in \mathbb{R}^6$, and $\Delta\mathbf{B}_2 \in \mathbb{R}^6$ are model uncertainty terms of the system. Set $\overline{d} \in \mathbb{R}^6$ as system compound disturbances including model uncertainty and external disturbances, and its expression is

$$\overline{d} = -\Delta\mathbf{M}\dot{e}_2 + \Delta\mathbf{B}_1 + \Delta\mathbf{B}_2 + \mathbf{d}. \tag{21}$$

*Assumption 1.* The chaser can obtain its own motion information $\{\mathbf{r}_c, \boldsymbol{\upsilon}_c, \boldsymbol{\sigma}_c, \boldsymbol{\omega}_c\}$ and relative motion information $\{\mathbf{r}_e, \boldsymbol{\upsilon}_e, \boldsymbol{\sigma}_e, \boldsymbol{\omega}_e\}$ through its own measurement device. The measured relative motion and relative attitude information are smooth and bounded.

*Assumption 2.* System compound disturbances $\overline{d} \in \mathbb{R}^6$ and its time derivative $\overline{d} \in \mathbb{R}^6$ are unknown but bounded.

The system compound disturbances $\overline{d} \in \mathbb{R}^6$ satisfies the following equation [33]:

$$\|\overline{\mathbf{d}}\| < k_0 + k_1\|\mathbf{e}_1\| + k_2\|\mathbf{e}_2\|^2, \tag{22}$$

where $k_0 > 0$, $k_1 > 0$, and $k_2 > 0$ are constants, and $\|\cdot\|$ represents the 2 norm of the vector.

Substituting equation (21) into (20) yields

$$\mathbf{M}_d\dot{\mathbf{e}}_2 = \mathbf{B}_{d1} + \mathbf{B}_{d2} + \mathbf{u} + \overline{\mathbf{d}}. \tag{23}$$

From equation (23) yields

$$\dot{\mathbf{e}}_2 = \mathbf{M}_p\left(\mathbf{B}_{d1} + \mathbf{B}_{d2}\right) + \mathbf{M}_p\mathbf{u} + \mathbf{M}_p\overline{\mathbf{d}}, \tag{24}$$

where $\mathbf{M}_p \in \mathbb{R}^{6\times6}$ is the generalized inverse matrix of $\mathbf{M}_d \in \mathbb{R}^{6\times6}$. The expression of $\mathbf{M}_p$ is

$$\mathbf{M}_p = \left(\mathbf{M}_d^{\mathrm{T}}\mathbf{M}_d\right)^{-1}\mathbf{M}_d^{\mathrm{T}}. \tag{25}$$

The time derivative of equation (17) gives

$$\ddot{\mathbf{e}}_1 = \dot{\mathbf{A}}_1\mathbf{e}_1 + \mathbf{A}_1\dot{\mathbf{e}}_1 + \dot{\mathbf{A}}_2\mathbf{e}_2 + \mathbf{A}_2\dot{\mathbf{e}}_2. \tag{26}$$

The time derivative of equation (24) gives

$$\ddot{\mathbf{e}}_2 = \frac{\mathrm{d}\left(\mathbf{M}_p\mathbf{B}_{d1} + \mathbf{M}_p\mathbf{B}_{d2}\right)}{\mathrm{d}t} + \dot{\mathbf{M}}_p\mathbf{u} + \mathbf{M}_p\dot{\mathbf{u}} + \mathbf{D}_1, \tag{27}$$

where $\mathbf{D}_1 = \dot{\mathbf{M}}_p\overline{d} + \mathbf{M}_p\dot{\overline{d}}$.

The sliding mode function is designed as

$$\mathbf{s} = \mathbf{e}_2 + \mathbf{c}\mathbf{e}_1, \tag{28}$$

where $\mathbf{c} \in \mathbb{R}^{6\times 6}$ is a sixth-order positive-definite diagonal matrix, $\mathbf{c} = \mathrm{diag}(c_1, \cdots, c_6)$, $c_i > 0, i = 1, 2, \cdots, 6$. From equation (28), it can be obtained that when $\mathbf{s} \longrightarrow \mathbf{0}$, then $\mathbf{e}_1 \longrightarrow \mathbf{0}$ and $\mathbf{e}_2 \longrightarrow \mathbf{0}$ as well.

The first derivative of the sliding mode function is

$$\dot{\mathbf{s}} = \dot{\mathbf{e}}_2 + \mathbf{c}\dot{\mathbf{e}}_1. \tag{29}$$

Substituting equations (17) and (24) into equation (29) yields

$$\dot{\mathbf{s}} = \mathbf{M}_p\left(\mathbf{B}_{d1} + \mathbf{B}_{d2} + \mathbf{u} + \overline{\mathrm{d}}\right) + \mathbf{c}\left(\mathbf{A}_1\mathbf{e}_1 + \mathbf{A}_2\mathbf{e}_2\right). \tag{30}$$

In this paper, the second-order nonsingular terminal sliding mode (NTSM) control theory is used to design the control law. In order to design a nonsingular terminal sliding mode (NTSM) controller, the nonsingular terminal sliding mode (NTSM) surface $\boldsymbol{\sigma}$ is defined as

$$\boldsymbol{\sigma} = \mathbf{s} + \boldsymbol{\beta}^{-1}\dot{\mathbf{s}}^{p/q}, \tag{31}$$

where $\boldsymbol{\beta} = \mathrm{diag}(\beta_1, \cdots, \beta_6)$, $\beta_i > 0, i = 1, 2, \cdots, 6$. $p > 0$ and $q > 0$ are odd integers and satisfy the condition $1 < p/q < 2$. In order to facilitate subsequent derivation, the following definition is made.

*Definition 1.* $\mathbf{G}^j\mathbf{H} = [G_1^jH_1, G_2^jH_2, \ldots, G_m^jH_m]^{\mathrm{T}}$ for any two vectors $\mathbf{G} = [G_1, G_2, \ldots, G_m]^{\mathrm{T}}$ and $\mathbf{H} = [H_1, H_2, \ldots, H_m]^{\mathrm{T}}$.

The time derivative of equation (31) gives

$$\begin{aligned}\dot{\boldsymbol{\sigma}} &= \dot{\mathbf{s}} + (p/q)\boldsymbol{\beta}^{-1}\dot{\mathbf{s}}^{p/q-1}\ddot{\mathbf{s}} \\ &= (p/q)\boldsymbol{\beta}^{-1}\dot{\mathbf{s}}^{p/q-1}\left(\ddot{\mathbf{s}} + (q/p)\boldsymbol{\beta}\dot{\mathbf{s}}^{2-p/q}\right).\end{aligned} \tag{32}$$

The time derivative of equation (29) gives

$$\begin{aligned}\ddot{\mathbf{s}} &= \ddot{\mathbf{e}}_2 + \mathbf{c}\ddot{\mathbf{e}}_1 \\ &= \frac{\mathrm{d}\left(\mathbf{M}_p\mathbf{B}_{d1} + \mathbf{M}_p\mathbf{B}_{d2}\right)}{\mathrm{d}t} + \dot{\mathbf{M}}_p\mathbf{u} + \mathbf{M}_p\dot{\mathbf{u}} + \mathbf{D}_1 + \mathbf{c}\left(\dot{\mathbf{A}}_1\mathbf{e}_1 + \mathbf{A}_1\dot{\mathbf{e}}_1 + \dot{\mathbf{A}}_2\mathbf{e}_2 + \mathbf{A}_2\dot{\mathbf{e}}_2\right) \\ &= \frac{\mathrm{d}\left(\mathbf{M}_p\mathbf{B}_{d1} + \mathbf{M}_p\mathbf{B}_{d2}\right)}{\mathrm{d}t} + \dot{\mathbf{M}}_p\mathbf{u} + \mathbf{M}_p\dot{\mathbf{u}} + \mathbf{c}\left(\mathbf{A}_1\left(\mathbf{A}_1\mathbf{e}_1 + \mathbf{A}_2\mathbf{e}_2\right) + \mathbf{A}_2\left(\mathbf{M}_p\mathbf{B}_{d1} + \mathbf{M}_p\mathbf{B}_{d2} + \mathbf{M}_p\mathbf{u} + \mathbf{M}_p\overline{d}\right)\right) \\ &\quad + \mathbf{c}\left(\dot{\mathbf{A}}_1\mathbf{e}_1 + \dot{\mathbf{A}}_2\mathbf{e}_2\right) + \mathbf{D}_1 \\ &= \frac{\mathrm{d}\left(\mathbf{M}_p\mathbf{B}_{d1} + \mathbf{M}_p\mathbf{B}_{d2}\right)}{\mathrm{d}t} + \left(\dot{\mathbf{M}}_p + \mathbf{c}\mathbf{A}_2\mathbf{M}_p\right)\mathbf{u} + \mathbf{M}_p\dot{\mathbf{u}} + \mathbf{c}\mathbf{A}_1\left(\mathbf{A}_1\mathbf{e}_1 + \mathbf{A}_2\mathbf{e}_2\right) + \mathbf{c}\left(\dot{\mathbf{A}}_1\mathbf{e}_1 + \dot{\mathbf{A}}_2\mathbf{e}_2\right) \\ &\quad + \mathbf{c}\mathbf{A}_2\left(\mathbf{M}_p\mathbf{B}_{d1} + \mathbf{M}_p\mathbf{B}_{d2}\right) + \mathbf{D},\end{aligned} \tag{33}$$

where $\mathbf{D} = \mathbf{c}\mathbf{A}_2\mathbf{M}_p\overline{\mathbf{d}} + \mathbf{D}_1$. According to equation (22) and Assumption 2 yield

$$\|\mathbf{D}\| = \left\|\mathbf{c}\mathbf{A}_2\mathbf{M}_p\overline{\mathbf{d}} + \mathbf{D}_1\right\| < D_0 + D_1\|\mathbf{e}_1\| + D_2\|\mathbf{e}_2\|^2, \tag{34}$$

where $D_0 > 0$, $D_1 > 0$, and $D_2 > 0$ are constants.

*Proof.* Lyapunov function $V_1$ is expressed as

$$V_1 = \frac{1}{2}\left(\boldsymbol{\sigma}^{\mathrm{T}}\boldsymbol{\sigma} + \lambda_0\tilde{D}_0^2 + \lambda_1\tilde{D}_1^2 + \lambda_2\tilde{D}_2^2\right), \tag{35}$$

where $\lambda_0 > 0$, $\lambda_1 > 0$, and $\lambda_2 > 0$ are constant parameters, $\tilde{D}_0 = \hat{D}_0 - D_0$, $\tilde{D}_1 = \hat{D}_1 - D_1$, and $\tilde{D}_2 = \hat{D}_2 - D_2$ are adaptation errors, and $\hat{D}_0$, $\hat{D}_1$, and $\hat{D}_2$ are the estimations of $D_0$, $D_1$, and $D_2$, respectively.

The time derivative of equation (35) gives

$$\begin{aligned}\dot{V}_1 &= \boldsymbol{\sigma}^{\mathrm{T}}\dot{\boldsymbol{\sigma}} + \lambda_0\tilde{D}_0\dot{\tilde{D}}_0 + \lambda_1\tilde{D}_1\dot{\tilde{D}}_1 + \lambda_2\tilde{D}_2\dot{\tilde{D}}_2 \\ &= \boldsymbol{\sigma}^{\mathrm{T}}(p/q)\boldsymbol{\beta}^{-1}\dot{\mathbf{s}}^{p/q-1}\left(\ddot{\mathbf{s}} + (q/p)\boldsymbol{\beta}\dot{\mathbf{s}}^{2-p/q}\right) + \lambda_0\left(\hat{D}_0 - D_0\right)\dot{\hat{D}}_0 + \lambda_1\left(\hat{D}_1 - D_1\right)\dot{\hat{D}}_1 + \lambda_2\left(\hat{D}_2 - D_2\right)\dot{\hat{D}}_2 \\ &= \boldsymbol{\sigma}^{\mathrm{T}}(p/q)\boldsymbol{\beta}^{-1}\dot{\mathbf{s}}^{p/q-1}\left\{\frac{\mathrm{d}\left(\mathbf{M}_p\mathbf{B}_{d1} + \mathbf{M}_p\mathbf{B}_{d2}\right)}{\mathrm{d}t} + \left(\dot{M}_p + \mathbf{c}\mathbf{A}_2\mathbf{M}_p\right)\mathbf{u} + \mathbf{M}_p\dot{\mathbf{u}} + \mathbf{c}\mathbf{A}_2\left(\mathbf{M}_p\mathbf{B}_{d1} + \mathbf{M}_p\mathbf{B}_{d2}\right) + \mathbf{D} + \mathbf{c}\mathbf{A}_1\left(\mathbf{A}_1\mathbf{e}_1 + \mathbf{A}_2\mathbf{e}_2\right)\right. \\ &\quad \left. + \mathbf{c}\left(\dot{\mathbf{A}}_1\mathbf{e}_1 + \dot{\mathbf{A}}_2\mathbf{e}_2\right) + (q/p)\boldsymbol{\beta}\dot{\mathbf{s}}^{2-p/q}\right\} + \lambda_0\left(\hat{D}_0 - D_0\right)\dot{\hat{D}}_0 + \lambda_1\left(\hat{D}_1 - D_1\right)\dot{\hat{D}}_1 + \lambda_2\left(\hat{D}_2 - D_2\right)\dot{\hat{D}}_2.\end{aligned} \tag{36}$$

The control law $\mathbf{u}$ is designed as

$$\mathbf{u} = \int_0^t \dot{\mathbf{u}}\,\mathrm{d}t, \tag{37}$$

$$\begin{aligned}\dot{\mathbf{u}} = & -\mathbf{M}_p^{-1}\left\{\frac{\mathrm{d}\left(\mathbf{M}_p\mathbf{B}_{d1}+\mathbf{M}_p\mathbf{B}_{d2}\right)}{\mathrm{d}t}+\left(\dot{\mathbf{M}}_p+\mathbf{c}\mathbf{A}_2\mathbf{M}_p\right)\mathbf{u}+\mathbf{c}\mathbf{A}_1\right.\\ & \cdot\left(\mathbf{A}_1\mathbf{e}_1+\mathbf{A}_2\mathbf{e}_2\right)+\mathbf{c}\left(\dot{\mathbf{A}}_1\mathbf{e}_1+\dot{\mathbf{A}}_2\mathbf{e}_2\right)+\mathbf{c}\mathbf{A}_2\\ & \cdot\left(\mathbf{M}_p\mathbf{B}_{d1}+\mathbf{M}_p\mathbf{B}_{d2}\right)+(q/p)\boldsymbol{\beta}\dot{\mathbf{s}}^{2-p/q}\\ & \left.+\left(\hat{D}_0+\hat{D}_1\|\mathbf{e}_1\|+\hat{D}_2\|\mathbf{e}_2\|^2\right)\mathrm{sgn}(\boldsymbol{\sigma})+\boldsymbol{\gamma}\boldsymbol{\sigma}\right\},\end{aligned} \tag{38}$$

where $\boldsymbol{\gamma}=\mathrm{diag}(\gamma_1,\cdots,\gamma_6)$, $\gamma_i>0, i=1,2,\cdots,6$.

The adaptation law $\hat{\dot{D}}_0$, $\hat{\dot{D}}_1$, and $\hat{\dot{D}}_2$ is designed as

$$\hat{\dot{D}}_0=\varepsilon_0(p/q)\|\boldsymbol{\beta}^{-1}\|\|\dot{\mathbf{s}}^{p/q-1}\boldsymbol{\sigma}^{\mathrm{T}}\|, \tag{39}$$

$$\hat{\dot{D}}_1=\varepsilon_1(p/q)\|\boldsymbol{\beta}^{-1}\|\|\dot{\mathbf{s}}^{p/q-1}\boldsymbol{\sigma}^{\mathrm{T}}\|\|\mathbf{e}_1\|, \tag{40}$$

$$\hat{\dot{D}}_2=\varepsilon_2(p/q)\|\boldsymbol{\beta}^{-1}\|\|\dot{\mathbf{s}}^{p/q-1}\boldsymbol{\sigma}^{\mathrm{T}}\|\|\mathbf{e}_2\|^2, \tag{41}$$

where $\varepsilon_0>0$, $\varepsilon_1>0$, and $\varepsilon_2>0$ are the tuning parameters.

Substituting equations (38)~(41) into equation (36) yields

$$\begin{aligned}\dot{V}_1=&\boldsymbol{\sigma}^{\mathrm{T}}(p/q)\boldsymbol{\beta}^{-1}\dot{\mathbf{s}}^{p/q-1}\left\{\mathbf{D}-\left(\hat{D}_0+\hat{D}_1\|\mathbf{e}_1\|+\hat{D}_2\|\mathbf{e}_2\|^2\right)\mathrm{sgn}(\boldsymbol{\sigma})-\boldsymbol{\gamma}\boldsymbol{\sigma}\right\}+\lambda_0\left(\hat{D}_0-D_0\right)\varepsilon_0(p/q)\|\boldsymbol{\beta}^{-1}\|\|\dot{\mathbf{s}}^{p/q-1}\boldsymbol{\sigma}^{\mathrm{T}}\|\\ &+\lambda_1\left(\hat{D}_1-D_1\right)\varepsilon_1(p/q)\|\boldsymbol{\beta}^{-1}\|\|\dot{\mathbf{s}}^{p/q-1}\boldsymbol{\sigma}^{\mathrm{T}}\|\|\mathbf{e}_1\|+\lambda_2\left(\hat{D}_2-D_2\right)\varepsilon_2(p/q)\|\boldsymbol{\beta}^{-1}\|\|\dot{\mathbf{s}}^{p/q-1}\boldsymbol{\sigma}^{\mathrm{T}}\|\|\mathbf{e}_2\|^2,\end{aligned} \tag{42}$$

then

$$\begin{aligned}\dot{V}_1\le&(p/q)\|\boldsymbol{\beta}^{-1}\|\|\dot{\mathbf{s}}^{p/q-1}\|\left\{\|\mathbf{D}\|\|\boldsymbol{\sigma}\|-\|\boldsymbol{\gamma}\|\|\boldsymbol{\sigma}\|^2-\left\|\left(\hat{D}_0+\hat{D}_1\|\mathbf{e}_1\|+\hat{D}_2\|\mathbf{e}_2\|^2\right)\right\|\|\boldsymbol{\sigma}\|+\lambda_0\varepsilon_0\|\hat{D}_0-D_0\|\|\boldsymbol{\sigma}\|+\lambda_1\varepsilon_1\|\hat{D}_1-D_1\|\|\boldsymbol{\sigma}\|\|\mathbf{e}_1\|\right.\\ &\left.+\lambda_2\varepsilon_2\|\hat{D}_2-D_2\|\|\boldsymbol{\sigma}\|\|\mathbf{e}_2\|^2\right\}\le(p/q)\|\boldsymbol{\beta}^{-1}\|\|\dot{\mathbf{s}}^{p/q-1}\|\left\{\|\mathbf{D}\|\|\boldsymbol{\sigma}\|-\|\boldsymbol{\gamma}\|\|\boldsymbol{\sigma}\|^2-\left\|\left(\hat{D}_0+\hat{D}_1\|\mathbf{e}_1\|+\hat{D}_2\|\mathbf{e}_2\|^2\right)\right\|\|\boldsymbol{\sigma}\|+\left\|\left(D_0+D_1\|\mathbf{e}_1\|\right.\right.\right.\\ &\left.\left.\left.+D_2\|\mathbf{e}_2\|^2\right)\right\|\|\boldsymbol{\sigma}\|-\left\|\left(D_0+D_1\|\mathbf{e}_1\|+D_2\|\mathbf{e}_2\|^2\right)\right\|\|\boldsymbol{\sigma}\|+\lambda_0\varepsilon_0\|\hat{D}_0-D_0\|\|\boldsymbol{\sigma}\|+\lambda_1\varepsilon_1\|\hat{D}_1-D_1\|\|\boldsymbol{\sigma}\|\|\mathbf{e}_1\|\right.\\ &\left.+\lambda_2\varepsilon_2\|\hat{D}_2-D_2\|\|\boldsymbol{\sigma}\|\|\mathbf{e}_2\|^2\right\}\le-(p/q)\|\boldsymbol{\beta}^{-1}\|\|\dot{\mathbf{s}}^{p/q-1}\|\left\{\left(\left\|\left(D_0+D_1\|\mathbf{e}_1\|+D_2\|\mathbf{e}_2\|^2\right)\right\|-\|\mathbf{D}\|\right)\|\boldsymbol{\sigma}\|\right.\\ &\left.-(1-\lambda_0\varepsilon_0)\|\hat{D}_0-D_0\|\|\boldsymbol{\sigma}\|-(1-\lambda_1\varepsilon_1)\|\hat{D}_1-D_1\|\|\boldsymbol{\sigma}\|\|\mathbf{e}_1\|-(1-\lambda_2\varepsilon_2)\|\hat{D}_2-D_2\|\|\boldsymbol{\sigma}\|\|\mathbf{e}_2\|^2\right\}\\ \le&-h_1\|\boldsymbol{\sigma}\|-h_2\|\hat{D}_0-D_0\|-h_3\|\hat{D}_1-D_1\|-h_4\|\hat{D}_2-D_2\|\le-h_1\sqrt{2}\,\frac{\|\boldsymbol{\sigma}\|}{\sqrt{2}}-h_2\sqrt{2\lambda_0}\,\frac{\|\tilde{D}_0\|}{\sqrt{2\lambda_0}}-h_3\sqrt{2\lambda_1}\,\frac{\|\tilde{D}_1\|}{\sqrt{2\lambda_1}}-h_4\sqrt{2\lambda_2}\,\frac{\|\tilde{D}_2\|}{\sqrt{2\lambda_2}},\end{aligned} \tag{43}$$

where

$$\begin{aligned}h_1&=(p/q)\|\boldsymbol{\beta}^{-1}\|\|\dot{\mathbf{s}}^{p/q-1}\|\left\{\left\|\left(D_0+D_1\|\mathbf{e}_1\|+D_2\|\mathbf{e}_2\|^2\right)\right\|-\|\mathbf{D}\|\right\},\\ h_2&=(p/q)\|\boldsymbol{\beta}^{-1}\|\|\dot{\mathbf{s}}^{p/q-1}\|\{(1-\lambda_0\varepsilon_0)\|\boldsymbol{\sigma}\|\},\\ h_3&=(p/q)\|\boldsymbol{\beta}^{-1}\|\|\dot{\mathbf{s}}^{p/q-1}\|\{(1-\lambda_1\varepsilon_1)\|\boldsymbol{\sigma}\|\|\mathbf{e}_1\|\},\\ h_4&=(p/q)\|\boldsymbol{\beta}^{-1}\|\|\dot{\mathbf{s}}^{p/q-1}\|\left\{(1-\lambda_2\varepsilon_2)\|\boldsymbol{\sigma}\|\|\mathbf{e}_2\|^2\right\}.\end{aligned} \tag{44}$$

So,

$$\begin{aligned}\dot{V}_1\le&-\min\left\{\sqrt{2}\,h_1,\ \sqrt{2/\lambda_0}\,h_2,\ \sqrt{2/\lambda_1}\,h_3,\ \sqrt{2/\lambda_2}\,h_4\right\}\\ &\cdot\left(\frac{\|\boldsymbol{\sigma}\|}{\sqrt{2}}+\sqrt{\frac{\lambda_0}{2}}\|\tilde{D}_0\|+\sqrt{\frac{\lambda_1}{2}}\|\tilde{D}_1\|+\sqrt{\frac{\lambda_2}{2}}\|\tilde{D}_2\|\right)\\ \le&-h\sqrt{V_1},\end{aligned} \tag{45}$$

where $h=\min\{\sqrt{2}\,h_1,\ \sqrt{2/\lambda_0}\,h_2,\ \sqrt{2/\lambda_1}\,h_3,\ \sqrt{2/\lambda_2}\,h_4\}$. According to equation (34), it can be known that $h_1>0$. In order to ensure $h_2>0$, $h_3>0$, and $h_4>0$, the condition $1-\lambda_0\varepsilon_0>0$, $1-\lambda_1\varepsilon_1>0$, and $1-\lambda_2\varepsilon_2>0$ must be satisfied when designing parameters.

$\|\dot{\mathbf{s}}^{p/q-1}\| > 0$ for any $\dot{\mathbf{s}} \neq \mathbf{0}$ and $\|\dot{\mathbf{s}}^{p/q-1}\| = 0$ only when $\dot{\mathbf{s}} = \mathbf{0}$. According to the accessibility condition of the sliding mode, the system can reach $\boldsymbol{\sigma} = \mathbf{0}$ from any initial state $\boldsymbol{\sigma}(0) \neq \mathbf{0}$ within a finite time $t_r$. Then, it will be proven that the sliding mode function $\mathbf{s}$ will also reach the $\mathbf{s} = \mathbf{0}$ plane in the finite time $t_s$ on the nonsingular terminal sliding mode surface $\boldsymbol{\sigma} = \mathbf{0}$. First, the lemma for the stability of a nonlinear system is given [49]. □

**Lemma 1.** *If there is a continuous function $V(t)$, the following conditions are met:*

*(1) $V(t)$ is positive*

*(2) There is a real number $\chi > 0$ and an open neighborhood $n \in (0, 1)$ so that*

$$\dot{V}(t) + \chi V^n(t) \leq 0. \tag{46}$$

Then, the system is stable in finite time, and the convergence time $t_f$ satisfies

$$t_f \leq \frac{1}{\chi(1-n)} V^{1-n}(0). \tag{47}$$

Lyapunov function $V_2$ is defined as

$$V_2 = \frac{1}{2}\mathbf{s}^{\mathrm{T}}\mathbf{s}. \tag{48}$$

On the nonsingular terminal sliding surface $\boldsymbol{\sigma} = \mathbf{0}$, the following equation can be obtained:

$$\boldsymbol{\sigma} = \mathbf{s} + \boldsymbol{\beta}^{-1}\dot{\mathbf{s}}^{p/q} = \mathbf{0}, \tag{49}$$

i.e.,

$$\dot{\mathbf{s}} = -(\boldsymbol{\beta}\mathbf{s})^{q/p}. \tag{50}$$

The time derivative of equation (48) gives

$$\dot{V}_2 = \mathbf{s}^{\mathrm{T}}\dot{\mathbf{s}}. \tag{51}$$

Substituting equation (50) in (51) yields

$$\begin{aligned}\dot{V}_2 &= -\mathbf{s}^{\mathrm{T}}\boldsymbol{\beta}^{q/p}\mathbf{s}^{p/q} \\ &\leq -\beta_{\min}^{q/p}\left(\sqrt{2}\,\frac{\|\mathbf{s}\|}{\sqrt{2}}\right)^{(p+q)/p} = -\beta_{\min}^{q/p}2^{(p+q)/2p}V_2^{(p+q)/2p} \\ &= -\chi_s V_2^{n_s}(t),\end{aligned} \tag{52}$$

i.e.,

$$\dot{V}_2 + \chi_s V_2^{n_s}(t) \leq 0, \tag{53}$$

where $\beta_{\min}$ is the smallest absolute component of $\boldsymbol{\beta}$, $\chi_s = \beta_{\min}^{q/p}2^{(p+q)/2p} > 0$, $n_s = (p+q/2p) \in (0,1)$.

Let the $\mathbf{s}$ converge to $\mathbf{0}$ within finite time $t_s$. It can be deduced from Lemma 1 that when $t \geq t_s$, $\mathbf{s}(\mathrm{t}) = \mathbf{0}$ and satisfies

$$t_s = t_r + \beta_{\min}^{-q/p}\frac{p}{p-q}\|\mathbf{s}(t_r)\|^{p-q/p}. \tag{54}$$

Since the sliding mode function $\mathbf{s}$ converges to $\mathbf{0}$ within finite time $t_s$, according to equation (49), $\boldsymbol{\sigma}$ will also converge to $\mathbf{0}$ within finite time $t_s$. It can be seen from equation (28) that if $\mathbf{s} \longrightarrow \mathbf{0}$, then $\mathbf{e}_1 \longrightarrow \mathbf{0}$ and $\mathbf{e}_2 \longrightarrow \mathbf{0}$. This case completes the proof.

The control system diagram with the adaptive nonsingular terminal sliding mode controller is shown in Figure 2.

From equation (38) yields

$$\begin{aligned}\dot{\mathbf{u}} + \mathbf{M}_p^{-1}\left(\dot{\mathbf{M}}_p + \mathbf{c}\mathbf{A}_2\mathbf{M}_p\right)\mathbf{u} = -\mathbf{M}_p^{-1}\Bigg\{&\frac{\mathrm{d}\left(\mathbf{M}_p\mathbf{B}_{d1} + \mathbf{M}_p\mathbf{B}_{d2}\right)}{\mathrm{d}t} + \mathbf{c}\mathbf{A}_1\left(\mathbf{A}_1\mathbf{e}_1 + \mathbf{A}_2\mathbf{e}_2\right) + \mathbf{c}\left(\dot{\mathbf{A}}_1\mathbf{e}_1 + \dot{\mathbf{A}}_2\mathbf{e}_2\right) + \mathbf{c}\mathbf{A}_2\left(\mathbf{M}_p\mathbf{B}_{d1} + \mathbf{M}_p\mathbf{B}_{d2}\right) \\ &+ (q/p)\boldsymbol{\beta}\dot{\mathbf{s}}^{2-p/q} + \left(\widehat{D}_0 + \widehat{D}_1\|\mathbf{e}_1\| + \widehat{D}_2\|\mathbf{e}_2\|^2\right)\mathrm{sgn}(\boldsymbol{\sigma}) + \boldsymbol{\gamma}\boldsymbol{\sigma}\Bigg\}.\end{aligned} \tag{55}$$

*Remark 2.* Equation (55) is essentially a low-pass filter with the right side of the equation as the input and $\mathbf{u}$ as the output. Therefore, the adaptive nonsingular terminal sliding mode (ANTSM) controller designed in this paper can eliminate the chattering phenomenon of the conventional sliding mode.

*Remark 3.* The parameters $\varepsilon_0$, $\varepsilon_1$, and $\varepsilon_2$ determine the rate at which the estimated values $\widehat{D}_0$, $\widehat{D}_1$, and $\widehat{D}_2$ converge to their respective boundaries. Larger $\varepsilon_0$, $\varepsilon_1$, and $\varepsilon_2$ ensure that the estimated values $\widehat{D}_0$, $\widehat{D}_1$, and $\widehat{D}_2$ quickly converge to the actual boundary $D_0$, $D_1$, and $D_2$. Considering $\lambda_0\varepsilon_0 < 1$, $\lambda_1\varepsilon_1 < 1$, and $\lambda_2\varepsilon_2 < 1$, the actual value is to weigh the convergence rate and constraints.

*Remark 4.* The parameter $\boldsymbol{\gamma}$ determines the convergence rate of the sliding surface. Larger $\boldsymbol{\gamma}$ means faster convergence rate, which requires larger input. In reality, the thrust of the spacecraft is limited. Therefore, the value of $\boldsymbol{\gamma}$ needs to be weighed between thrust condition and convergence rate.

*Remark 5.* The proposed methodology is applicable when $\|\boldsymbol{\sigma}\|$ is reachable. However, $\|\boldsymbol{\sigma}\|$ cannot become exactly 0 in a finite time due to nonlinear characteristics of the system and the switching delays. Therefore, the adaptive parameters $\widehat{D}_0$, $\widehat{D}_1$, and $\widehat{D}_2$ may become boundless. A simple method is to use the dead zone to overcome the above difficulties, and the adaptive law $\widehat{D}_0$, $\widehat{D}_1$, and $\widehat{D}_2$ of equations (39)~(41) are modified as

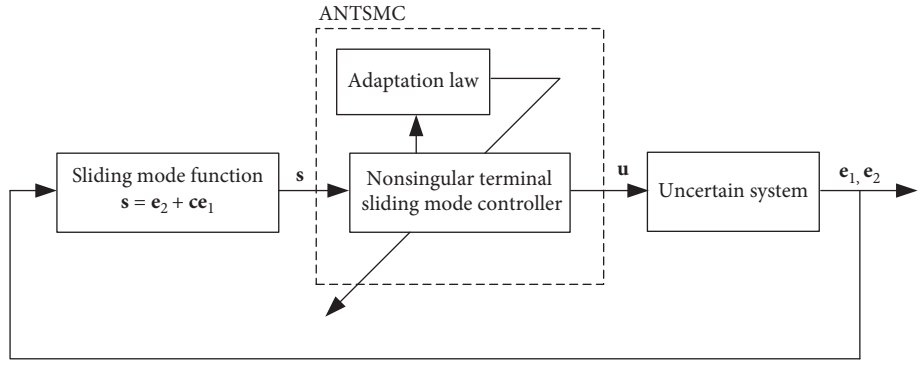


Figure 2: Control system diagram.

$$\dot{\hat{D}}_0 = \begin{cases} \varepsilon_0 (p/q) \left\| \boldsymbol{\beta}^{-1} \right\| \left\| \dot{\mathbf{s}}^{p/q-1} \boldsymbol{\sigma}^{\mathrm{T}} \right\|, & \|\boldsymbol{\sigma}\| \geq \mu, \\ 0, & \|\boldsymbol{\sigma}\| < \mu, \end{cases}$$

$$\dot{\hat{D}}_1 = \begin{cases} \varepsilon_1 (p/q) \left\| \boldsymbol{\beta}^{-1} \right\| \left\| \dot{\mathbf{s}}^{p/q-1} \boldsymbol{\sigma}^{\mathrm{T}} \right\| \left\| \mathbf{e}_1 \right\|, & \|\boldsymbol{\sigma}\| \geq \mu, \\ 0, & \|\boldsymbol{\sigma}\| < \mu, \end{cases} \tag{56}$$

$$\dot{\hat{D}}_2 = \begin{cases} \varepsilon_2 (p/q) \left\| \boldsymbol{\beta}^{-1} \right\| \left\| \dot{\mathbf{s}}^{p/q-1} \boldsymbol{\sigma}^{\mathrm{T}} \right\| \left\| \mathbf{e}_2 \right\|^2, & \|\boldsymbol{\sigma}\| \geq \mu, \\ 0, & \|\boldsymbol{\sigma}\| < \mu. \end{cases}$$

Table 1: Simulation parameters.

| Variable | Value |
|---|---|
| $\mathbf{h}_f$ | $[0, 5, 0]^{\mathrm{T}}$ |
| $\mathbf{r}_c(t_0)$/m | $[-2.0449, 4.6646, 4.4429]^{\mathrm{T}} \times 10^6$ |
| $\boldsymbol{\upsilon}_c(t_0)$/(m/s) | $[-4.6536, -5.1599, 3.2906]^{\mathrm{T}} \times 10^3$ |
| $\boldsymbol{\sigma}_c(t_0)$ | $[0, 0, 0]^{\mathrm{T}}$ |
| $\boldsymbol{\omega}_c(t_0)$/(rad/s) | $[0, 0, 0]^{\mathrm{T}}$ |
| $\mathbf{r}_e(t_0)$/m | $[30, 0, 25]^{\mathrm{T}}$ |
| $\boldsymbol{\upsilon}_e(t_0)$/(m/s) | $[0.8, -0.6, 0.3]^{\mathrm{T}}$ |
| $\boldsymbol{\sigma}_e(t_0)$ | $[0.4, -0.5, 0.6]^{\mathrm{T}}$ |
| $\boldsymbol{\omega}_e(t_0)$/(rad/s) | $[-0.0207, 0.0125, 0.0258]^{\mathrm{T}}$ |

## 4. Simulation Example

This section verifies the effectiveness of the designed controller through simulation of a chaser's superclose distance hovering over a noncooperative target. The mass of the chaser is $m_c = 58.2\,\mathrm{kg}$. The moments of inertia of the target and chaser, $\mathbf{J}_t$ and $\mathbf{J}_c$, are [30]

$$\mathbf{J}_t = \begin{bmatrix} 3336.3 & -135.4 & -154.2 \\ -135.4 & 3184.5 & -148.5 \\ -154.2 & -148.5 & 2423.7 \end{bmatrix} \mathrm{kg{\cdot}m^2},$$

$$\mathbf{J}_{\mathrm{c}} = \begin{bmatrix} 598.3 & -22.5 & -51.5 \\ -22.5 & 424.4 & -27 \\ -51.5 & -27 & 263.6 \end{bmatrix} \mathrm{kg{\cdot}m^2}. \tag{57}$$

The model uncertainties are $\Delta m_c = 0.5\,\mathrm{kg}$ and $\Delta \mathbf{J}_{\mathrm{c}} = \begin{bmatrix} 1.7 & 2 & 1.5 \\ 2.5 & 4.4 & 3 \\ 1.5 & -27 & 3.6 \end{bmatrix} \mathrm{kg{\cdot}m^2}$.

The hovering position in the frame $F_T$ is $\mathbf{h}_f$. The initial position and velocity are $\mathbf{r}_c(t_0)$ and $\boldsymbol{\upsilon}_c(t_0)$, respectively. The initial attitude and angular velocity are $\boldsymbol{\sigma}_c(t_0)$ and $\boldsymbol{\omega}_c(t_0)$, respectively. The initial relative position and relative velocity are $\mathbf{r}_e(t_0)$ and $\boldsymbol{\upsilon}_e(t_0)$, respectively. The initial relative attitude and relative angular velocity are $\boldsymbol{\sigma}_e(t_0)$ and $\boldsymbol{\omega}_e(t_0)$, respectively. The values of the above parameters are listed in Table 1.

Disturbance torque $\boldsymbol{\tau}_d$ and disturbance force $\mathbf{F}_d$ are

$$\boldsymbol{\tau}_d = \begin{bmatrix} 1 - 3\sin(\omega_0 t) - 2\cos(\omega_0 t) \\ 3 + 2\sin(\omega_0 t) + \cos(\omega_0 t) \\ 2 - 3\sin(\omega_0 t) + 3\cos(\omega_0 t) \end{bmatrix} \times 10^{-5}\mathrm{Nm},$$

$$\mathbf{F}_d = \begin{bmatrix} 2 - 3\sin(\omega_0 t) + \cos(\omega_0 t) \\ 1 + 3\sin(\omega_0 t) + 2\cos(\omega_0 t) \\ 3 - 2\sin(\omega_0 t) - 2\cos(\omega_0 t) \end{bmatrix} \times 10^{-4}\mathrm{N}, \tag{58}$$

where $\omega_o = \sqrt{\mu / \|\mathbf{r}_c\|^3}$ is the chaser's average orbital angular velocity, and $\mu = 3.986 \times 10^{14}\,\mathrm{m^3/s^2}$ is the gravitational constant of the Earth.

The controller parameters are selected as $\mathbf{c} = \mathrm{diag}(0.1, 0.1, 0.1, 0.1, 0.1, 0.1)$, $p = 5$, $q = 3$, $\boldsymbol{\beta} = \mathrm{diag}(0.2, 0.2, 0.2, 0.1, 0.1, 0.1)$, $\boldsymbol{\gamma} = \mathrm{diag}(90, 90, 90, 3, 3, 3)$, $\varepsilon_0 = 1 \times 10^{-5}$, $\varepsilon_1 = 3 \times 10^{-5}$, $\varepsilon_2 = 3 \times 10^{-5}$, $\hat{D}_0(0) = 0$, $\hat{D}_1(0) = 0$, $\hat{D}_2(0) = 0$, and $\mu = 0.001$. The simulation results are presented in Figures 3 and 4.

Figure 3 shows relative motion, control torque, and control force. The relative attitude drops from $[0.4, -0.5, 0.6]^{\mathrm{T}}$ to $\mathbf{0}_{3\times1}$ after 58 s; the relative angular velocity increased rapidly from $[-0.0207, 0.0125, 0.0258]^{\mathrm{T}}$ rad/s and then decreased to $\mathbf{0}_{3\times1}$ rad/s after

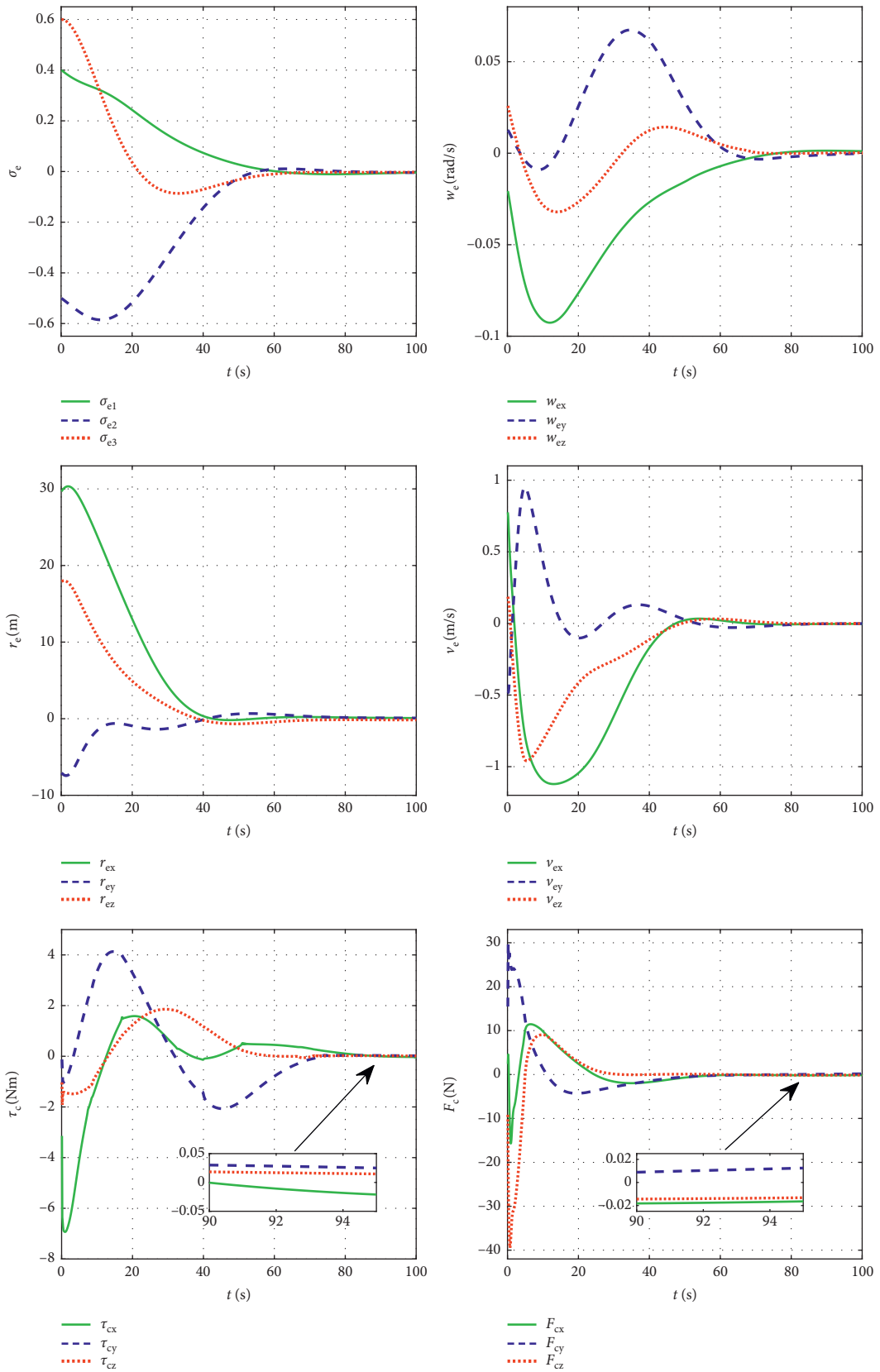


Figure 3: Relative motion, control torque and, control force.

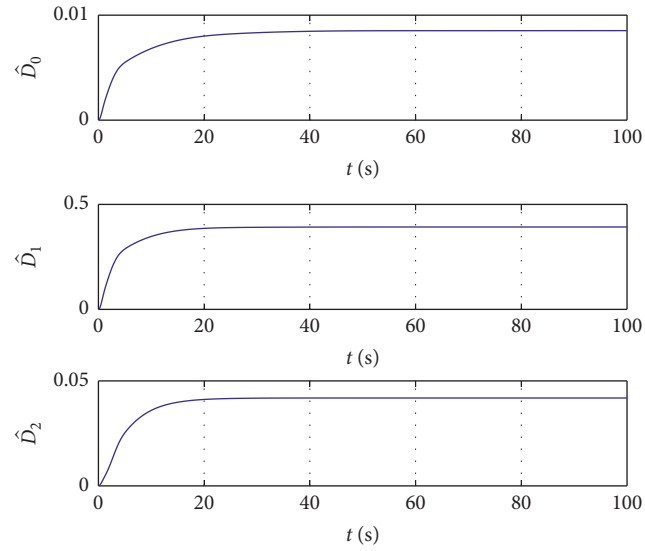


Figure 4: Estimated parameters $\widehat{D}_0$, $\widehat{D}_1$, and $\widehat{D}_2$ using the adaptive tuning method.

reaching the peak value, which indicates that the chaser completes attitude capture for the noncooperative target and then maintains the attitude synchronization with the target. After 71 s, the relative position drops from $[30, -7, 18]^{\mathrm{T}}$ m to $\mathbf{0}_{3\times1}$ m and the relative velocity drops from $[0.776, -0.485, 0.186]^{\mathrm{T}}$ m/s to $\mathbf{0}_{3\times1}$ m/s. It is indicated that the chaser's center of mass has reached the desired hovering position in the frame $F_T$ and has remained unchanged thereafter. The control torque required by the chaser is minimal after 73 s, and the maximum control torque in each direction does not exceed 0.05 Nm. The control force required by the chaser is minimal after 48 s, and the maximum control force in each direction does not exceed 0.2 N. The chaser's control torque and control force curve are smooth throughout the entire process, indicating no chattering occurs. Figure 4 shows estimated parameters $\widehat{D}_0$, $\widehat{D}_1$, and $\widehat{D}_2$ using the adaptive tuning method. $\widehat{D}_0$, $\widehat{D}_1$, and $\widehat{D}_2$ finally converge to 0.0085, 0.3925, and 0.0419.

In order to verify the effectiveness of the proposed controller, it is necessary to compare it with the conventional sliding mode controller. The conventional sliding mode controller is chosen as [50]

$$\mathbf{u} = -\mathbf{M}_d\mathbf{c}\left(\mathbf{A}_1\mathbf{e}_1 + \mathbf{A}_2\mathbf{e}_2\right) - \mathbf{B}_{d1} - \mathbf{B}_{d2} - \mathbf{K}\,\mathrm{sgn}\left(\mathbf{s}\right). \quad (59)$$

The parameter of the conventional sliding mode controller is $\mathbf{K} = \mathrm{diag}(0.2, 0.2, 0.2, 0.2, 0.2, 0.2)$, and all other simulation parameters are the same as those of the proposed sliding mode controller. The simulation results are presented in Figure 5. By further comparing Figure 5 with Figure 3, it can be concluded that under the effect of the conventional sliding mode controller, the chaser finishes the attitude synchronization with the target and reaches the hovering point need 59 s and 74 s , respectively, which is 1 s and 3 s longer than the proposed sliding mode controller. After reaching the hovering position and completing the attitude synchronization, the maximum control torque and maximum control force required by the chaser in each direction are still as high as 0.5 Nm and 0.8 N, respectively. Chattering phenomenon occurs in both control torque and control force of the conventional sliding mode controller.

In addition, for the mean performance error index $\mathrm{MPE} = 1/T\sqrt{\int_0^T \|\mathbf{X}_e\|^2 \mathrm{d}t}$, the tracking error is $\mathbf{X}_e = [\mathbf{r}_e^{\mathrm{T}}, \mathbf{v}_e^{\mathrm{T}}, \boldsymbol{\sigma}_e^{\mathrm{T}}, \boldsymbol{\omega}_e^{\mathrm{T}}]^{\mathrm{T}}$ and the simulation time is $T = 100$ s. It can be calculated that the proposed controller is $\mathrm{MPE}_1 = 1.2550$, and the conventional sliding mode controller is $\mathrm{MPE}_2 = 1.4340$. Obviously, the proposed controller effectively improves the closed-loop system dynamic response performance.

In order to investigate the robustness of the proposed controller, the external bounded disturbance force $\mathbf{F}_d$ and torque $\boldsymbol{\tau}_d$ are increased to $100\mathbf{F}_d$ and $100\boldsymbol{\tau}_d$, respectively. Other simulation parameters are the same. The simulation results are presented in Figures 6 and 7. By comparing Figures 6 and 7 with Figures 3 and 4, it can be found that the chaser finishes the position synchronization at the hovering point after 71 s and finishes the attitude synchronization with the target after 58 s. The estimated parameters $\widehat{D}_0$, $\widehat{D}_1$, and $\widehat{D}_2$ finally converge to 0.0085, 0.3926, and 0.0419. The control torque and control force curve are smooth without chattering, and the mean performance error index is $\mathrm{MPE}_3 = 1.2551$. Compared with the small disturbance, the difference in control performance is very small, thus proving the strong robustness of the proposed sliding mode controller.

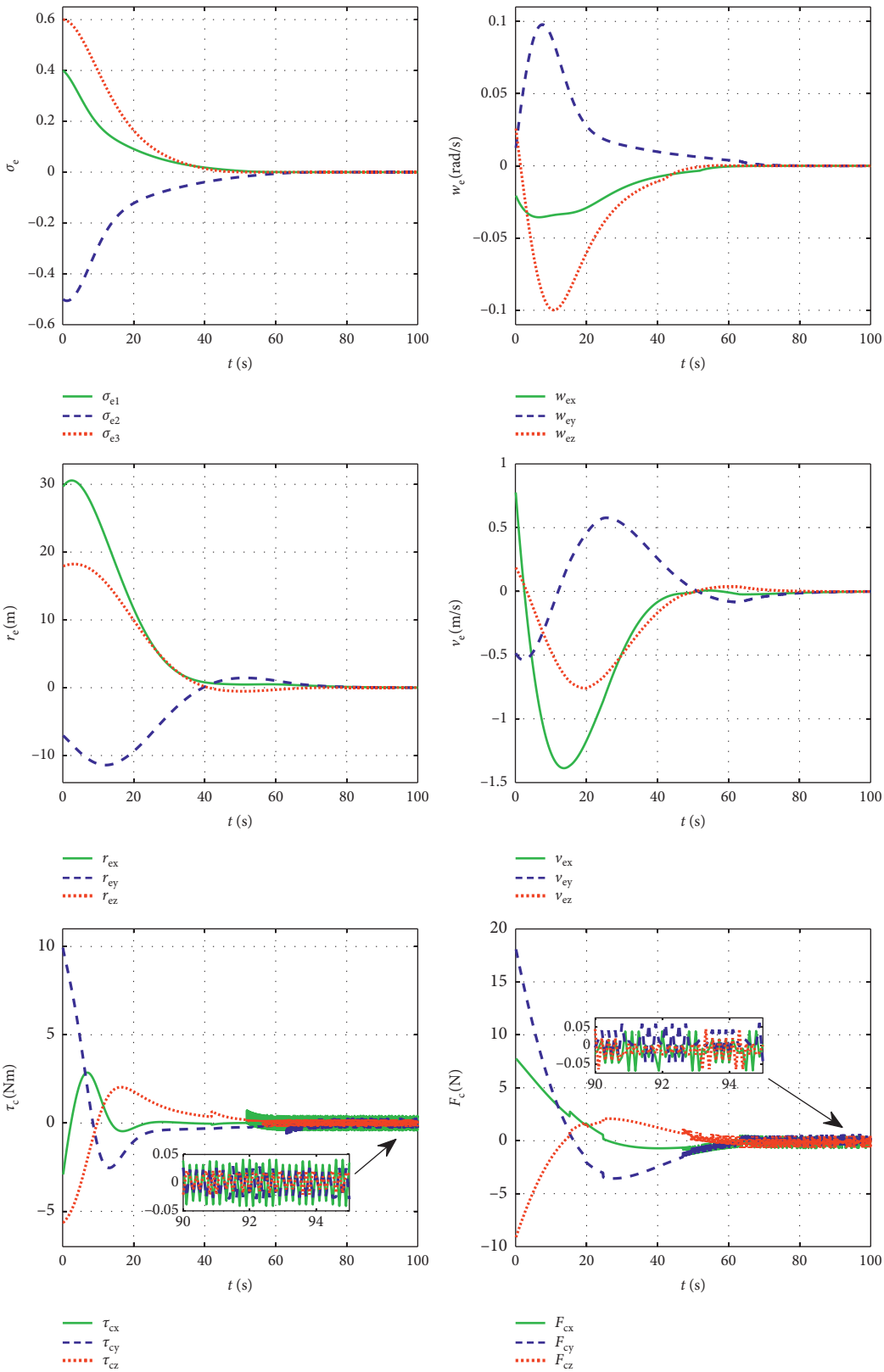


Figure 5: Relative motion, control torque, and control force under conventional sliding mode control.

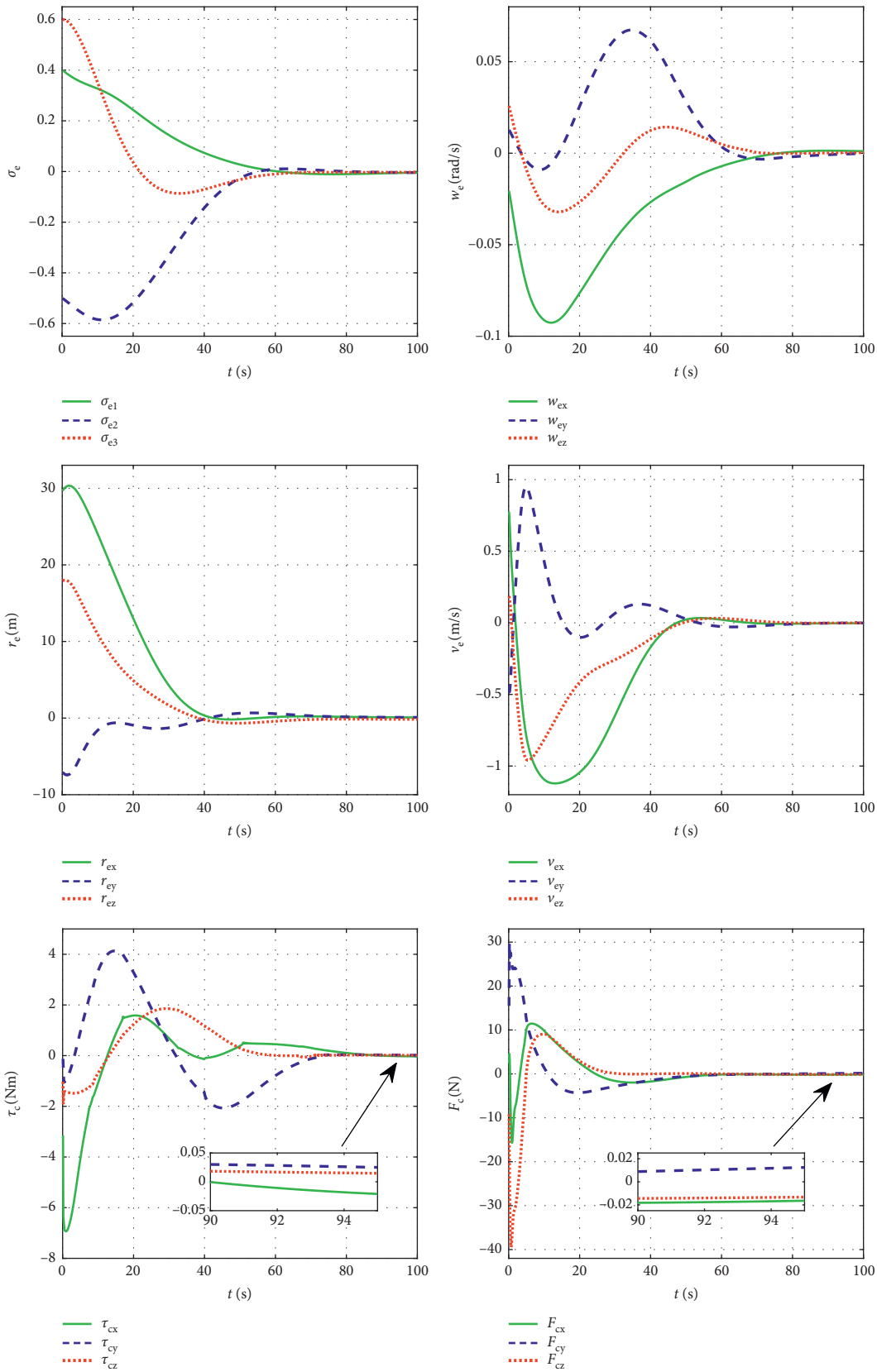


Figure 6: Relative motion, control torque, and control force under large disturbance.

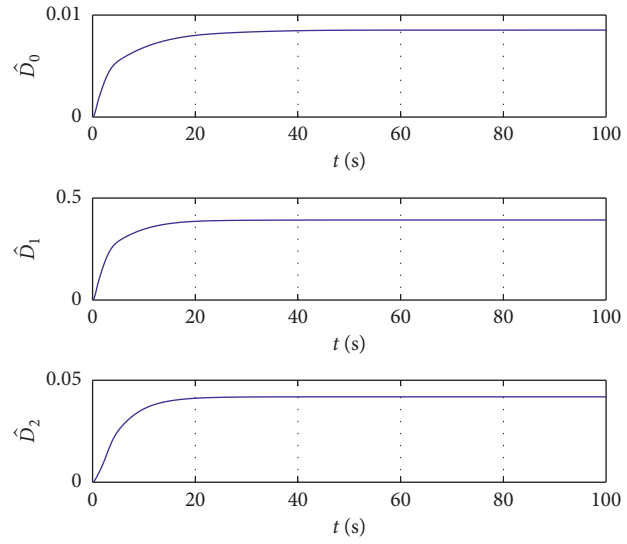


FIGURE 7: Estimated parameters $\hat{D}_0$, $\hat{D}_1$, and $\hat{D}_2$ using the adaptive tuning method under large disturbance.

## 5. Conclusions

In this paper, an adaptive nonsingular terminal sliding mode controller is designed based on the measurable information when the chaser hovers over a noncooperative target, and the six-degrees-of-freedom-coupled relative position and relative attitude control are realized. Instead of the conventional control input, its time derivative is used in the controller. The derivative control contains the discontinuous sign function, and the actual control input is obtained by integration, so it is continuous and chatter-free. The adaptive tuning method is used to deal with the model uncertainty and external disturbances. Simulation results show that the controller can effectively overcome the model uncertainty and the influence of external disturbance factors. The chaser quickly reaches the hovering position of the noncooperative target, and both the hovering position error and the hovering velocity error converge to a smaller range. The required control torque and control force are minimally, continuously, and smoothly produced with no chattering occurring.

## Data Availability

The data used to support the findings of this study are included within the article.

## Conflicts of Interest

The authors declare that they have no conflicts of interest.

## Acknowledgments

The authors are grateful to Prof. Li and Scholar Hao for discussions. The paper was supported by the National Natural Science Foundation of China (no. 11472301) and the Foundation of National University of Defense Technology (no. ZK18-03-07).

## References

[1] D. Wang, P. Huang, and Z. Meng, "Coordinated stabilization of tumbling targets using tethered space manipulators," *IEEE Transactions on Aerospace and Electronic Systems*, vol. 51, no. 3, pp. 2420–2432, 2015.

[2] S. Bandyopadhyay, S. J. Chung, and F. Y. Hadaegh, "Nonlinear attitude control of spacecraft with a large captured object," *Journal of Guidance, Control, and Dynamics*, vol. 39, no. 4, pp. 754–769, 2016.

[3] L. Zhang, S. Qian, S. Zhang, and H. Cai, "Research on angles-only/SINS/CNS relative position and attitude determination algorithm for a tumbling spacecraft," *Proceedings of the Institution of Mechanical Engineers, Part G: Journal of Aerospace Engineering*, vol. 231, no. 2, pp. 218–228, 2017.

[4] M. Wang, J. Luo, J. Yuan, and U. Walter, "Detumbling strategy and coordination control of kinematically redundant space robot after capturing a tumbling target," *Nonlinear Dynamics*, vol. 92, no. 3, pp. 1023–1043, 2018.

[5] Y. She, J. Sun, S. Li, W. Li, and T. Song, "Quasi-model free control for the post-capture operation of a non-cooperative target," *Acta Astronautica*, vol. 147, pp. 59–70, 2018.

[6] K. B. Li, W. S. Su, and L. Chen, "Performance analysis of differential geometric guidance law against high-speed target with arbitrarily maneuvering acceleration," *Proceedings of the Institution of Mechanical Engineers, Part G: Journal of Aerospace Engineering*, vol. 223, no. 10, pp. 3547–3563, 2019.

[7] D. J. Scheeres, "Stability of hovering orbits around small bodies," *Advances in the Astronautical Sciences*, vol. 102, pp. 855–875, 1999.

[8] S. B. Broschart and D. J. Scheeres, "Control of hovering spacecraft near small bodies: application to asteroid 25143 Itokawa," *Journal of Guidance, Control, and Dynamics*, vol. 28, no. 2, pp. 343–354, 2005.

[9] D. J. Scheeres, *Orbital Motion in Strongly Perturbed Environments*, Springer, Berlin, Heidelberg, Germany, 2012.

[10] S. Sawai, D. J. Scheeres, and S. B. Broschart, "Control of hovering spacecraft using altimetry," *Journal of Guidance Control & Dynamics*, vol. 25, no. 4, pp. 786–795, 2002.

[11] S. B. Broschart and D. J. Scheeres, "Boundedness of spacecraft hovering under dead-band control in time-Invariant systems," *Journal of Guidance, Control, and Dynamics*, vol. 30, no. 2, pp. 601–610, 2007.

[12] X. Zeng, S. Gong, J. Li, and K. T. Alfriend, "Solar sail body-fixed hovering over elongated asteroids," *Journal of Guidance Control & Dynamics*, vol. 39, no. 6, 2016.

[13] T. Kubota, T. Hashimoto, M. Uo, M. Maruya, and K. Baba, "Maneuver strategy for sta-tion keeping and global mapping around an asteroid AIAA/AAS spaceflight mechanics," *Advances in the Astronautical Sciences*, vol. 108, pp. 769–780, 2001.

[14] B. Gaudet and R. Furfaro, "Robust spacecraft hovering near small bodies in envi-ronments with unknown dynamics using reinforcement learning," in *Proceedings of the AIAA/AAS Astrodynamics Specialist Conference, AIAA 2012-5072*, Minneapolis, MN, USA, August 2012.

[15] K. Berry, B. Suttery, A. Mayz et al., "OSIRIS-REx Touch-And-Go (TAG) mission design and analysis," in *Proceedings of the 36th Annual AAS Guidance and Control Conference, AAS 13-095*, Breckenridge, CO, USA, February 2013.

[16] D. Lee, A. K. Sanyal, E. A. Butcher, and D. J. Scheeres, "Almost global asymptotic tracking control for spacecraft body-fixed hovering over an asteroid," *Aerospace Science and Technology*, vol. 38, no. 1, pp. 105–115, 2014.

[17] D. Lee, A. K. Sanyal, E. A. Butcher et al., "Spacecraft hovering control for body-fixed hovering over a uniformly rotating asteroid using geometric mechanics," *Advances in the Astronautical Sciences*, vol. 150, pp. 1757–1773, 2014.

[18] D. Lee, A. Sanyal, E. Butcher, and D. Scheeres, "Finite-time control for spacecraft body-fixed hovering over an asteroid," *IEEE Transactions on Aerospace and Electronic Systems*, vol. 51, no. 1, pp. 506–520, 2015.

[19] T. Tan and H. Wu, "Analytical solution method for orbit rendezvous, hovering and fly-around control," *Journal of Astronautic*, vol. 37, no. 11, pp. 1333–1341, 2016.

[20] T. Tan, "Full state feedback control of rendezvous, hovering and fly-around in elliptical orbit," *Journal of Astronautic*, vol. 37, no. 7, pp. 811–818, 2016.

[21] B. Xue, Z. She, J. Yu et al., "Control on the spacecraft hovering based on hybrid systems," *Chinese Space Science & Technology*, vol. 30, no. 2, pp. 61–67, 2010.

[22] B. Cheng, J. Yuan, and W. Ma, "Spacecraft multiple pulse hovering method based on state transition matrix," *Chinese Space Science & Technology*, vol. 36, no. 5, pp. 81–87, 2016.

[23] W. Xu, H. Wu, S. Lu et al., "Spacecraft attitude-orbit combined control analysis for flying-around and hovering task in super-close relative distance," in *Proceedings of the 32nd Chinese Control Conference*, Xi'an, China, July 2013.

[24] X. Song, L. Fan, Y. Chen et al., "Study of close-loop hovering method at any selected position to space target," *Chinese Space Science & Technology*, vol. 30, no. 1, pp. 41–45, 2010.

[25] Z. Dang, Z. Wang, and Y. Zhang, "Modeling and analysis of relative hovering control for spacecraft," *Journal of Guidance, Control, and Dynamics*, vol. 37, no. 4, pp. 1091–1102, 2014.

[26] X. Huang, Y. Yan, and Z. Huang, "Finite-time control of underactuated spacecraft hovering," *Control Engineering Practice*, vol. 68, pp. 46–62, 2017.

[27] D. Lee and G. Vukovich, "Robust adaptive terminal sliding mode control on SE(3) for autonomous spacecraft rendezvous and docking," *Nonlinear Dynamics*, vol. 83, no. 4, pp. 2263–2279, 2016.

[28] H. Yan, S. Tan, and Y. Xie, "Integrated translational and rotational control for the final approach phase of rendezvous and docking," *Asian Journal of Control*, vol. 20, no. 5, pp. 1967–1978, 2018.

[29] S. Zhu, R. Sun, J. Wang, J. Wang, and X. Shao, "Robust model predictive control for multi-step short range spacecraft rendezvous," *Advances in Space Research*, vol. 62, no. 1, 2018.

[30] L. Sun and Z. Zheng, "Adaptive relative pose control for autonomous spacecraft rendezvous and proximity operations with thrust misalignment and model uncertainties," *Advances in Space Research*, vol. 59, no. 7, pp. 1861–1871, 2017.

[31] L. Sun, W. Huo, and Z. Jiao, "Disturbance-observer-based robust relative pose control for spacecraft rendezvous and proximity operations under input saturation," *IEEE Transactions on Aerospace and Electronic Systems*, vol. 54, no. 4, pp. 1605–1617, 2018.

[32] L. Sun, W. He, and C. Sun, "Adaptive fuzzy relative pose control of spacecraft during rendezvous and proximity maneuvers," *IEEE Transactions on Fuzzy Systems*, vol. 26, no. 6, pp. 3440–3451, 2018.

[33] L. Sun and Z. Zheng, "Adaptive relative pose control of spacecraft with model couplings and uncertainties," *Acta Astronautica*, vol. 143, pp. 29–36, 2018.

[34] M. Zak, "Terminal attractors for addressable memory in neural networks," *Physics Letters A*, vol. 133, no. 1-2, pp. 18–22, 1988.

[35] M. Zhihong, A. P. Paplinski, and H. R. Wu, "A robust MIMO terminal sliding mode control scheme for rigid robotic manipulators," *IEEE Transactions on Automatic Control*, vol. 39, no. 12, pp. 2464–2469, 1994.

[36] K. B. Park and T. Tsuji, "Terminal sliding mode control of second-order nonlinear uncertain systems," *International Journal of Robust & Nonlinear Control*, vol. 9, no. 11, pp. 769–780, 1999.

[37] Y. Feng, X. Yu, and Z. Man, "Non-singular terminal sliding mode control of rigid manipulators," *Automatica*, vol. 38, no. 12, pp. 2159–2167, 2002.

[38] Y. Feng, X. Yu, and F. Han, "On nonsingular terminal sliding-mode control of nonlinear systems," *Automatica*, vol. 49, no. 6, pp. 1715–1722, 2013.

[39] S. Mondal and C. Mahanta, "Adaptive second order terminal sliding mode controller for robotic manipulators," *Journal of the Franklin Institute*, vol. 351, no. 4, pp. 2356–2377, 2014.

[40] R. Mohammadi Asl, Y. Shabbouei Hagh, and R. Palm, "Robust control by adaptive non-singular terminal sliding mode," *Engineering Applications of Artificial Intelligence*, vol. 59, pp. 205–217, 2017.

[41] A. Safa, R. Y. Abdolmalaki, S. Shafiee, and B. Sadeghi, "Adaptive nonsingular terminal sliding mode controller for micro/nanopositioning systems driven by linear piezoelectric ceramic motors," *ISA Transactions*, vol. 77, pp. 122–132, 2018.

[42] L. C. Maria and C. Andrea, "Nonsingular terminal sliding-mode control of nonlinear planar systems with global fixed-time stability guarantees," *Automatica*, vol. 95, pp. 561–565, 2018.

[43] L. Haibo, W. Heping, and S. Junlei, "Attitude control for QTR using exponential nonsingular terminal sliding mode control," *Journal of Systems Engineering and Electronics*, vol. 30, no. 1, pp. 195–204, 2019.

[44] Y. Wang, X. Zhang, X. Yuan, and G. Liu, "Position-sensorless hybrid sliding-mode control of electric vehicles with brushless DC motor," *IEEE Transactions on Vehicular Technology*, vol. 60, no. 2, pp. 421–432, 2011.

[45] Z. Xiaolei, Z. Yan, G. Kai, G. Li, and N. Deng, "An adaptive B-spline neural network and its application in terminal sliding mode control for a mobile satcom antenna inertially stabilized platform," *Sensors*, vol. 17, no. 5, pp. 978–998, 2017.

[46] J. Liu, H. Li, Y. Luo, and J. Zhang, "Robust adaptive relative position and attitude integrated control for approaching uncontrolled tumbling spacecraft," *Proceedings of the Institution of Mechanical Engineers, Part G: Journal of Aerospace Engineering*, pp. 1–14, 2019.

[47] M. Xin and H. Pan, "Nonlinear optimal control of spacecraft approaching a tumbling target," *Aerospace Science and Technology*, vol. 15, no. 2, pp. 79–89, 2011.

[48] M. D. Shuster, "A survey of attitude representation," *The Journal of the Astronautical Sciences*, vol. 41, no. 4, pp. 439–517, 1993.

[49] E. Moulay and W. Perruquetti, "Finite time stability conditions for non-autonomous continuous systems," *International Journal of Control*, vol. 81, no. 5, pp. 797–803, 2008.

[50] D. Feng, H. Jian, Y. Wang, J. Zhang, and S. He, "Sliding mode control with an extended disturbance observer for a class of underactuated system in cascaded form," *Nonlinear Dynamics*, vol. 90, no. 4, pp. 2571–2582, 2017.